Experimental and Numerical Investigation on the Interaction between Hydraulic Fractures and Vugs in Fracture-Cavity Carbonate Reservoirs

Lei Wang [1] , Xiaolong Wu [2],*, Longfei Hou [3], Yintong Guo [1] , Zhenhui Bi [1] and Hanzhi Yang [2]

[1] State Key Laboratory of Geomechanics and Geotechnical Engineering, Institute of Rock and Soil Mechanics, Chinese Academy of Sciences, Wuhan 430071, China

[2] State Key Laboratory of Coal Mine Disaster Dynamics and Control, Chongqing University, Chongqing 400044, China

[3] Guangzhou Expressway Co., Ltd., Guangzhou 510290, China

*   Correspondence: 202020021020@cqu.edu.cn; Tel.: +86-185-7151-3966 or +86-027-8719-8651

Abstract: In karstic-fractured carbonate reservoirs, most of the oil resources are hosted in vugs. Connecting as many vugs as possible by hydraulic fracturing is the key to achieving effective development. However, the interaction mechanism between vugs and hydraulic fractures is complicated and has not been fully revealed. In this study, both experimental and numerical simulations were implemented to investigate the interaction between vugs and hydraulic fractures. Key factors, such as vug size, horizontal stress difference, and the internal pressure of the vug, were considered. The results showed that the vug played an important role in the propagation of hydraulic fractures. Three interaction modes of vugs and hydraulic fractures were observed: crossing, arresting, and bypassing. Owing to the variation of the stress concentration existing around the vug, the hydraulic fracture could be arrested by a small vug but would bypass a vug with a larger size. Whether the hydraulic fracture could communicate with the vug was mainly controlled by the horizontal stress difference. Under large horizontal stress differences ($\geq$20 MPa), the hydraulic fracture could cross and connect multiple vugs. The difference between the horizontal minimum stress and the internal pressure of the vug was also particularly significant for fracture propagation. The smaller the difference, the easier the fracture communicated with the vug. The above findings would be valuable and constructive for the optimal design of field hydraulic fracturing in karstic-fractured carbonate reservoirs.

Keywords: carbonate reservoir; vug; hydraulic fracture propagation; physical simulation; XFEM model

1. Introduction

Carbonate reservoirs contain abundant oil and gas resources, and the output accounts for approximately 60% of the total global production. Consequently, carbonate oil and gas fields have become an essential component of oil and gas exploration and the economic development in various countries [1–3]. Owing to their low permeability, the reservoirs need stimulation to achieve commercial development [4]. Hydraulic fracturing has been effectively applied to carbonate reservoirs as a production enhancement method [5,6]. According to the field logging data, carbonate reservoirs contain a sizable number of vugs, which provide space for oil and gas to deposit [7–10]. The objective of hydraulic fracturing is to communicate with vugs via hydraulic fractures in order to maximize oil and gas recovery [11]. Therefore, it is critical to investigate the interaction between hydraulic fractures and vugs.

Focusing on the interaction between hydraulic fractures and vugs, many scholars have conducted related studies. For the specimens containing only one vug, three principal mechanisms of vug–hydraulic fracture interaction were observed: crossing, arrest, and bypassing [12]. Meanwhile, the pressure curve response is obvious with the interaction

between the vug and the hydraulic fracture. Furthermore, in specimens with evenly distributed cavities and randomly distributed natural cracks, three main modes of natural cavity connections exist: connections through straight main fractures, connections through curved main fractures, and connections through pre-existing cracks [13].

In addition to laboratory tests, numerical simulation tools can better enable us to comprehend the interactions between fractures and vugs. In a two-dimensional linear-elastic finite element model, Bittencourt et al. developed a solution for the quasi-automatic simulation of arbitrary crack extension [14]. Based on this strategy, Phongthanapanich et al. introduced a new adaptive Delaunay global triangular finite element method to improve the accuracy of fracture tip calculation results [15]. However, the finite element simulation methods require re-meshing, which increases the computer burden, whereas the extended finite element method (XFEM) avoids this disadvantage. Häusler introduced an innovative method for simulating fracture extension that combines the material force idea and the extended finite element method [16]. Sukumar et al. simulated cavities without specifying the internal borders by introducing a level set function to XFEM [17]. Owing to the existence of holes, there were severe stress concentrations in their vicinity, which changed the propagation direction of hydraulic fractures [18]. In fractured-vuggy carbonate reservoirs, the in situ stress difference plays a critical role in determining how effective hydraulic fracturing is [19]. When the difference of horizontal in situ stress is small, the hydraulic fracture cannot communicate with the vug. Additionally, increasing the fluid viscosity and injection rate could reduce the influence of the vug, whereas larger lateral stress coefficients enhance the vug's influence [20]. Intra-vug fluid pressure could reduce the degree of fracture path deflection [21]. Meanwhile, natural cracks near the hole would guide the expansion of hydraulic cracks and increase the possibility of penetrating the hole [18]. Other scholars have also conducted related studies using other methods [22–24]. Research is still needed in order to fully understand how hydraulic fractures and vugs interact with each other.

In general, hydraulic fractures usually propagate in the direction perpendicular to the minimum principal stress [25]. Unknown fracture extensions can, however, develop for other reasons such as preexisting fractures, rock inhomogeneity, and stress anisotropy [26,27]. Hydraulic fracture propagation can be controlled using the directional hydraulic fracturing technique [28,29].

In this study, the interaction of hydraulic fractures and vugs during directional fracturing is investigated. First, physical simulation tests of hydraulic fracturing in true triaxial stress conditions were conducted, taking vug size and horizontal stress difference into account. Furthermore, the extended finite element method was used to study the effects of other parameters, such as internal pressure in the vug, and multiple vugs. We focused on analyzing the key factors affecting the vug–hydraulic fracture interaction. The results can serve as a guide for the effective development of fractured-vuggy carbonate reservoirs.

2. Experimental Process and Scheme

2.1. Sample Preparation

For the convenience of vug prefabrication, artificial samples were chosen for testing. The samples were prepared using 40–80 mesh quartz sand and Portland cement (model 525) with a 1:1 mass ratio. The mechanical tests were conducted using the recommended ISRM methods to acquire the basic mechanical properties of the sample. The tensile strength, unconfined compressive strength, Young's modulus, and Poisson's ratio were 5.1 MPa, 64.1 MPa, 11.48 GPa, and 0.16, respectively.

The cubic samples with a length of 300 mm were prepared for the fracturing tests, as shown in Figure 1. After the raw materials were mixed, the cement slurry was poured into a 300 mm cube mold. During the casting procedure, an improved wellbore with an outer diameter of 20 mm, an inner diameter of 15 mm, and a length of 180 mm was positioned in the middle of the sample. At the 135–165 mm position of the wellbore, two 1.5 mm wide grooves were cut symmetrically to form the hydraulic channel. Two

thin plastic plates, 30 mm long and 20 mm wide, were inserted into the grooves to serve as the prefabricated fracture, guiding the directional propagation of hydraulic fractures (Figure 1a). The top 10 mm of the wellbore was threaded to connect with the pump line of the hydraulic fracturing pumping system, while the bottom was welded and sealed. Moreover, eggs of various sizes were positioned as prefabricated vugs on one or both sides of the wellbore (Figure 1b). After curing for 3 days, the specimens were removed from the mold and continued to cure for 15–20 days to ensure the stable strength of the specimens. The prepared sample is shown in Figure 1c.
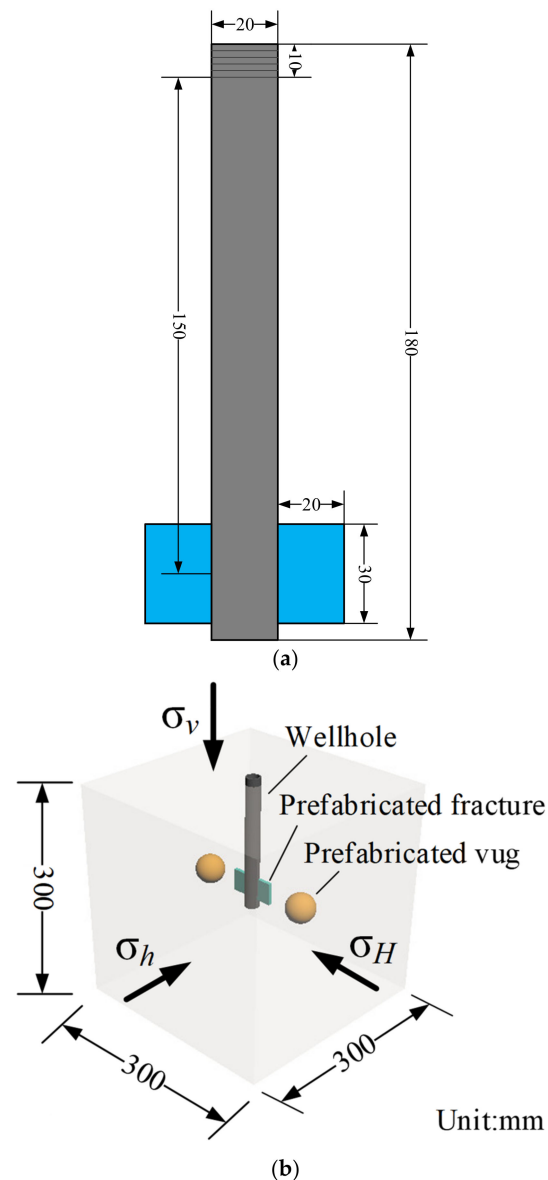

(a)

(b)

Figure 1. *Cont.*

(**c**)

Figure 1. Details of sample preparation: (**a**) wellbore design; (**b**) sample schematic diagram; and (**c**) a typical prepared sample.

2.2. Testing Equipment

The directional fracturing experiments were performed by a true triaxial hydraulic fracturing test system (Figure 2). The system contains a large-scale true triaxial testing machine and a hydraulic fracturing pumping system. The large-scale true triaxial testing machine is servo-controlled and can provide compressive stresses with a maximum load of 8000 kN in three mutually perpendicular directions independently. Its function is to simulate the in situ stress state in deep formations. The hydraulic fracturing pumping system, which has a maximum fluid injection pressure of 140 MPa and a maximum permissible injection volume of 800 mL, is used to inject the fracturing fluid. It can achieve pressure and displacement control. The controlled flow rate range is 0.01–10 mL/min. The parameters related to the above two subsystems were controlled and real-time recorded by computer. The system is qualified for simulating the initiation and propagation of hydraulic fracture under different test conditions.
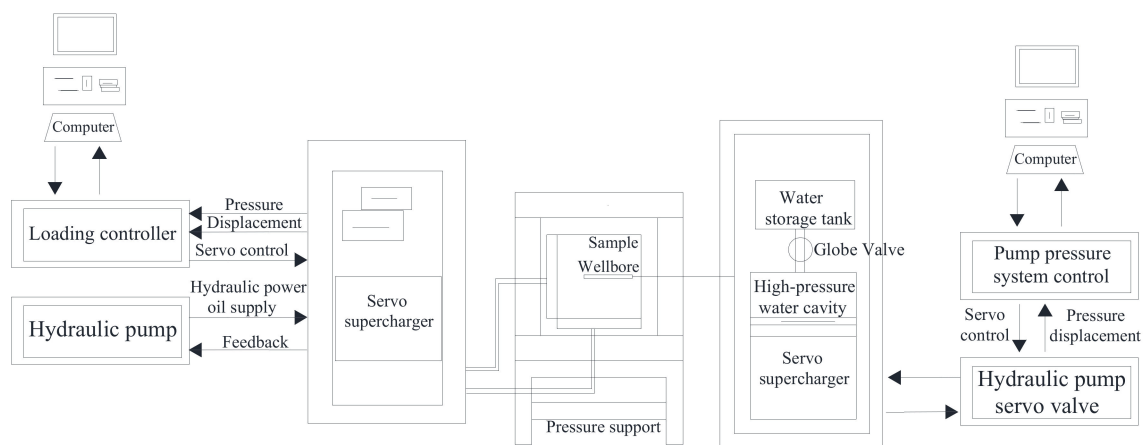

Figure 2. The true triaxial hydraulic fracturing test system.

2.3. Experimental Scheme

To investigate the interaction between the hydraulic fracture and the vug, two factors, including vug size and horizontal stress difference, were considered in the experimental

design. Quail eggs (3 cm × 2.5 mm), native eggs (6 cm × 4 mm), and eggs (7 cm × 5 mm) were chosen as the small, middle, and large sizes of vugs, respectively. Three horizontal stress differences ($\sigma_H - \sigma_h$ = 2, 3, 4 MPa) were studied. Pumping rate and fluid viscosity in each test were 5 mL/min and 100 mPa·s, respectively. The detailed experimental parameters are listed in Table 1.

Table 1. Experimental parameters in laboratory hydraulic fracturing.

Sample Number	$\sigma_v/\sigma_H/\sigma_h$ (MPa)	Pumping Rate (mL/min)	Fluid Viscosity (mPa·s)	Vug Size	The Vug-Hydraulic Fracture InterAction	Breakdown Pressure (MPa)
C-1	18/15/13	5	100	/	/	16.3
C-2	18/15/13	5	100	Small	Arrest	14.6
C-3	18/15/13	5	100	Middle	Arrest	17.2
C-4	18/15/13	5	100	Large	Bypassing	20.3
C-5	18/15/12	5	100	Large	Arrest	17.6
C-6	18/15/11	5	100	Large	Crossing	15.4

2.4. Test Procedure

The typical experimental procedures are as follows:

(1)　The prepared sample was placed in the true triaxial chamber. Then, the wellbore was connected to the injection line of the hydraulic fracturing pumping system.

(2)　The triaxial stresses were loaded independently from three mutually perpendicular directions to simulate in situ stresses based on the predetermined stress values. The triaxial stresses were loaded concurrently and then to diverse stress levels. This loading method eliminated the mechanical shear damage to the specimen caused by imbalanced loading.

(3)　Fracturing fluid was injected into the specimen at a given pumping rate, while the data acquisition system was activated synchronously to collect the data during the test. It should be noted that a type of red tracer had been mixed into the fracturing fluid to identify the propagation range of hydraulic fractures.

(4)　The pressure curve was analyzed to judge the start and propagation behavior of a hydraulic fracture during the test. After the test was completed, the sample was split to describe the hydraulic fracture propagation morphology.

3. Experimental Results and Analysis

3.1. The Morphology of the Hydraulic Fracture

3.1.1. The Effect of Vug Size

To investigate the effect of vug size on hydraulic fracture propagation, four groups of tests were examined. The results showed that the vug size plays a significant effect on the vug–hydraulic fracture interaction behaviors.

The hydraulic fracture morphology without prefabricated vug of sample C-1 is shown in Figure 3. The hydraulic fracture initiated from the wellbore and then extended along the prefabricated fracture path to the specimen boundary. Since the specimen did not contain any prefabricated vug, the hydraulic fracture propagation behavior was simple, leading in a complete and symmetrical rupture surface.
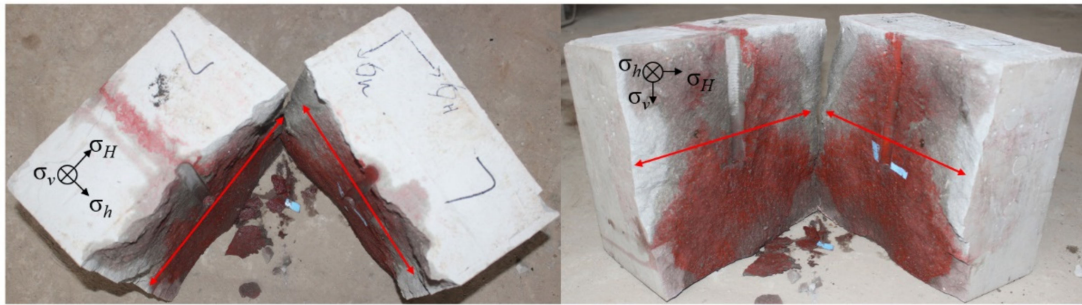
Figure 3. Hydraulic fracture geometry of sample C-1.

A prefabricated vug with a small size was placed on the right side of wellbore in sample C-2. As shown in Figure 4, the hydraulic fracture propagated in a plane along the maximum horizontal stress direction after the initiation from the wellbore. When the fracture encountered the vug, it was arrested by the vug. Then, the hydraulic fracture bypassed the vug and extended from the lower part of the vug to the sample boundary.
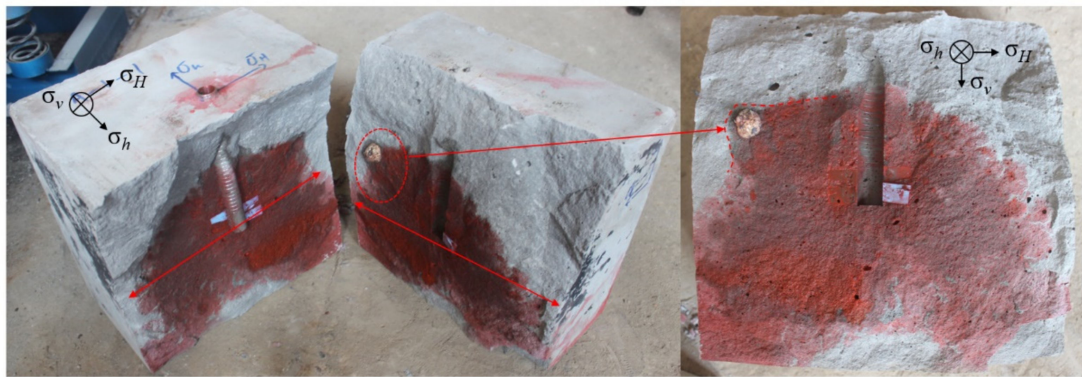

Figure 4. Hydraulic fracture geometry of sample C-2.

Similarly, in sample C-3, a middle-sized vug was prefabricated on the right side of the wellbore. As shown in Figure 5, the hydraulic fracture was deflected in the direction of the maximum horizontal stress, presenting a slight S-shape. When the hydraulic fracture encountered the vug, the further extension of the hydraulic fracture was prevented, which led to the continued propagation of the hydraulic fracture from both sides of the vug.

Figure 5. Hydraulic fracture geometry of sample C-3.

In sample C-4, a large vug on the right side of the wellbore was prepared for the test. The hydraulic fracture morphology of sample C-4 is presented in Figure 6. The hydraulic fracture was deflected with a greater angle in the direction of the maximum horizontal stress and its propagation range was concentrated in the bottom part of the

wellbore, according to the distribution of red tracer. The hydraulic fracture deflected near the wellbore, bypassed the vug, and extended to the sample boundary.
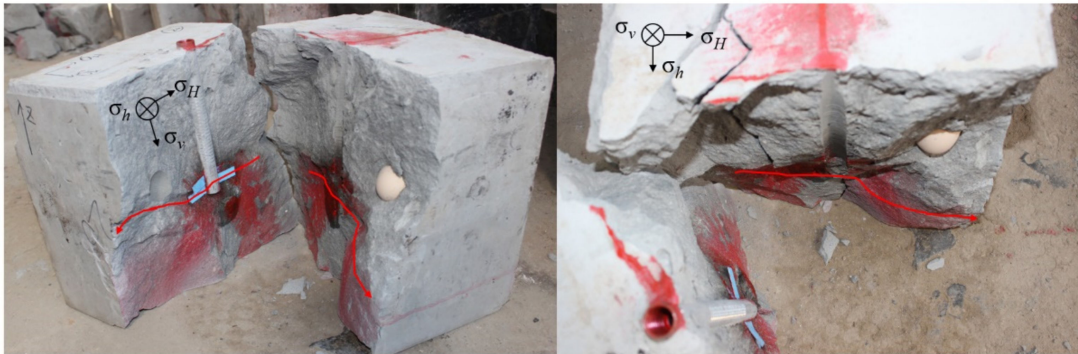

Figure 6. Hydraulic fracture geometry of sample C-4.

From what has been described in the results from each experimental sample (sample C-1, sample C-2, sample C-3, and sample C-4), it could be seen that the vug size exerted an important effect on the interaction between the vug and the hydraulic fracture. For samples C-2 and C-3, the hydraulic fractures were arrested by the small or medium-size vug. By contrast, in sample C-4, the hydraulic fracture bypassed the large vug during the fracturing process.

3.1.2. The Effect of Horizontal Stress Difference

Three groups of tests were conducted to investigate the effect of horizontal stress difference on the interaction between vugs and hydraulic fractures. Compared with specimen C-4, the vug conditions of specimens C-5 and C-6 were the same, while the horizontal stress difference increased from 2 MPa to 3 MPa and 4 MPa. The results revealed that the horizontal stress difference certainly had an influence on the vug–hydraulic fracture interaction behaviors.

Figure 7 provides the geometry of the hydraulic fracture of sample C-5. The hydraulic fracture gradually propagated to both sides along the prefabricated fracture after the initiation from the wellbore. On the one side of the wellbore, the hydraulic fracture encountered a large vug and stopped further propagation. For the other side without a vug, the hydraulic fracture propagated to the sample boundary on a plane. Compared with the result at $\sigma_H - \sigma_h = 2$ MPa, the interaction between the vug and the hydraulic fracture transformed from bypassing to arresting at $\sigma_H - \sigma_h = 3$ MPa, which indicated that the barrier effect of the vug was weakened.

Figure 7. Hydraulic fracture geometry of sample C-5.

With the horizontal stress difference further increasing to 4 MPa, the hydraulic fracture initiated from the wellbore and crossed the vug directly during the propagation process

(Figure 8). It was demonstrated that the large vug had little impact on fracture propagation with a horizontal stress difference of 4 MPa.
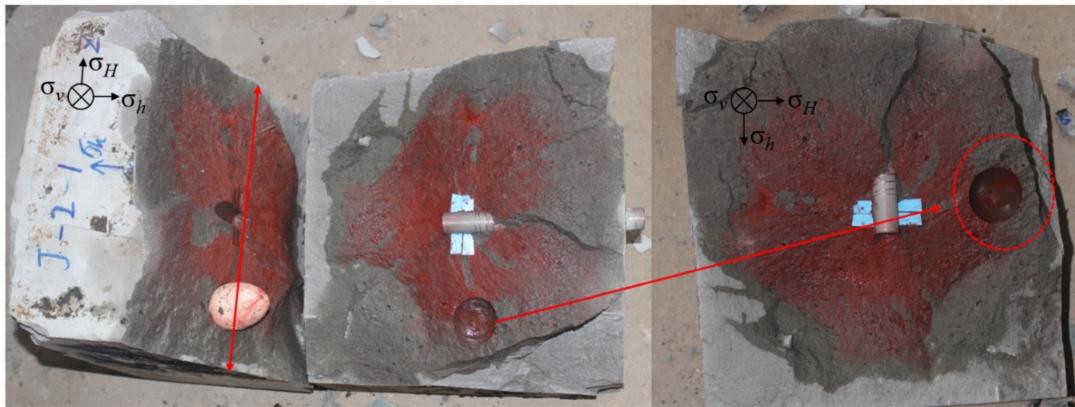

Figure 8. Hydraulic fracture geometry of sample C-6.

By comparing the results of the three samples (C-4, C-5, and C-6), it could be seen that the horizontal stress difference had an important influence on the propagation behavior of the hydraulic fracture. Under the condition of high horizontal stress difference, the hydraulic fracture geometry was straight and could penetrated the vug. When the horizontal stress difference decreased, the hydraulic fracture would be more deflected, and it was easy for hydraulic fractures to be arrested by the vug to stop the propagation or bypass the vug to further extension.

3.1.3. The Vug-Hydraulic Fracture Interaction

Six groups of directional hydraulic fracturing tests were successfully conducted to investigate the vug–hydraulic fracture interaction in artificial samples. During the test, the experimental results were different depending on the vug size and horizontal stress difference of each specimen. The collected test results are shown in Table 1.

The experimental results showed that the vug exerts a significant impact on the behavior of hydraulic fracture propagation. As illustrated in Figure 9, three main vug–hydraulic fracture interaction patterns were observed.

(1) Crossing: the hydraulic fracture directly crossed the vug at relatively large vug size and big horizontal stress difference.
(2) Arresting: the hydraulic fracture was arrested by the vug at small to middle vug size and middle horizontal stress difference.
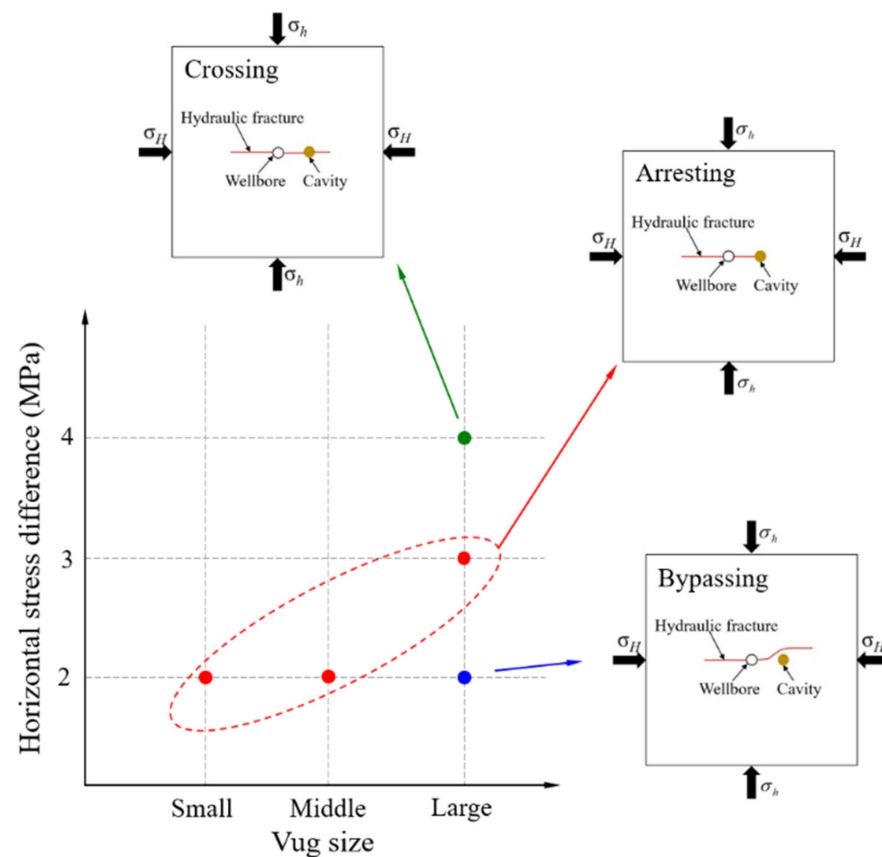(3) Bypassing: the hydraulic fracture bypassed the vug at large vug size and small horizontal stress difference.

Figure 9. Three patterns of interaction between vug and hydraulic fracture.

3.2. Characteristics of the Pressure Curves

For laboratory and field hydraulic fracturing operations, the characteristics of hydraulic fracture initiation and propagation can be reflected in pressure curves. How the pressure curve reacted to the interaction between hydraulic fracture and vug was described and analyzed in the following section.

3.2.1. The Effect of Vug Size

The pressure curves of samples C-1 to C-4 were plotted in Figure 10a. For the sample without vug (C-1), the shape of pressure curve o was conventional, corresponding to the simple morphology of the hydraulic fracture. The pressure curve of sample C-2 with a small vug was similar to that of sample C-1: growing rapidly to the breakdown pressure, dropping sharply, and finally maintaining relatively stable. For the specimens C-3 and C-4 with relatively middle- and large-sized vugs, remarkable pressure fluctuation was observed following the breakdown stage, reflecting the interaction between the hydraulic fracture and the vug during the extension. With the increase of vug size, the duration of pressure curve fluctuation became longer.

The evolution of breakdown pressure was also shown in Figure 10b. With the increase of vug size, the initiation of the hydraulic fracture became more difficult, leading to the gradual increase of breakdown pressure. The average increase amplitude of breakdown pressure is 24.66%. The fluctuation stage of pressure and increase of breakdown pressure were helpful to understand the effect of the vug size on the vug-hydraulic fracture interaction.
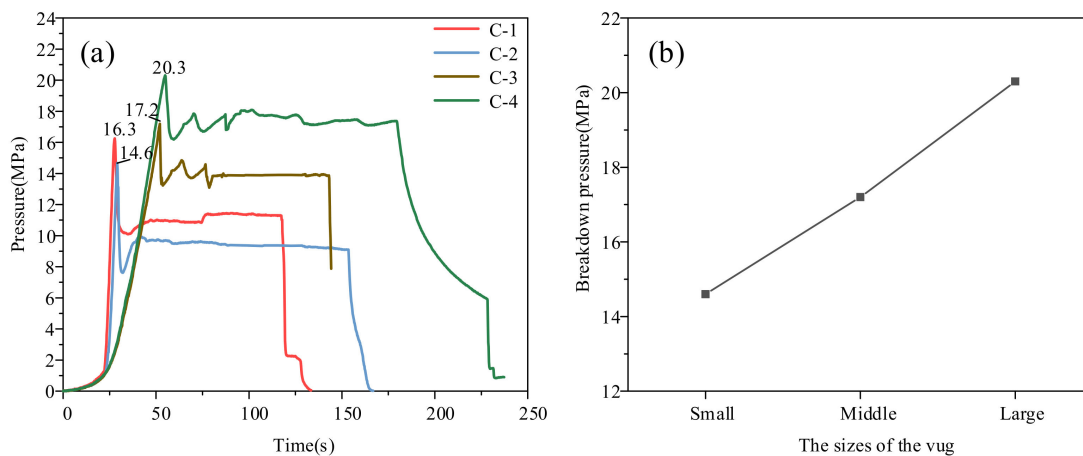
Figure 10. Pressure curves and breakdown pressures for different vug sizes: (**a**) pressure curves and; (**b**) breakdown pressures.

3.2.2. The Effect of Horizontal Stress Differences

The pressure curves under different horizontal stress differences are illustrated in Figure 11a. The pressure of specimen C-5 reached a peak of 17.6 MPa and gradually stabilized after a large drop. Unlike specimen C-5, the pressure of specimen C-6 decreased from the maximum value of 15.4 MPa, displaying a rising and then falling trend, which might reflect the vug–hydraulic fracture interaction.

The breakdown pressure and its variation under different horizontal stress differences are drawn in Figure 11b. With the decrease of horizontal minimum stress, the difficulty of initiation of the hydraulic fracture decreased, leading to the gradual decrease of breakdown pressure. The average decrease in the amplitude of breakdown pressure was 14.82%.
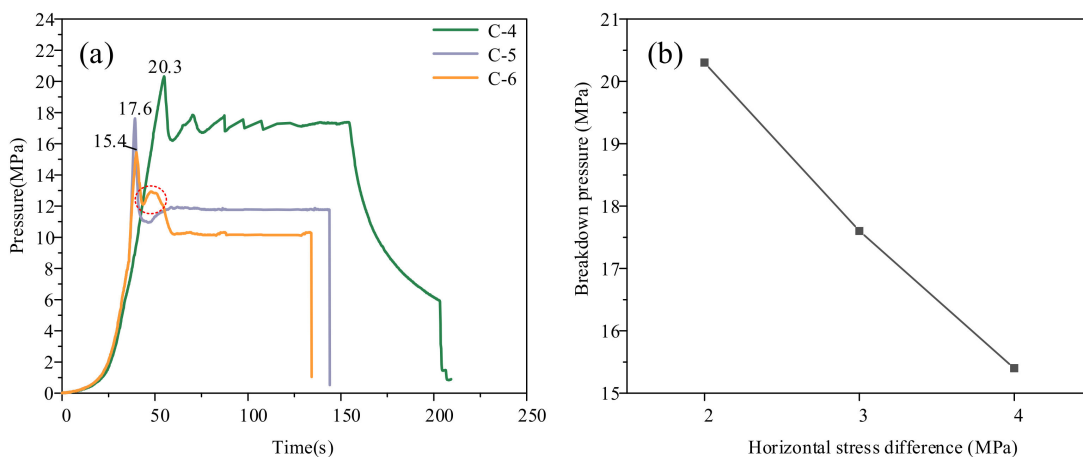

Figure 11. Pressure curves and breakdown pressures for different horizontal stress differences: (**a**) pressure curves and (**b**) breakdown pressures. (The red circle reflected the interaction between the vug and the hydraulic fracture.).

4. Numerical Simulation

4.1. Establishment of a Fluid–Solid Coupling Mathematical Model

4.1.1. Equilibrium and Continuity Equation

The mechanical equilibrium equation of porous medium rock can be expressed by the principle of virtual work. The stress balance, without considering the viscosity of the fluid, is expressed as [30]:

$$\int_V \delta\varepsilon^T D_{ep} \frac{d\varepsilon}{dt} dV + \int_V \delta\varepsilon^T D_{ep} \left[m \frac{(s_o + p_o\varepsilon)}{3K_s} \frac{dp_o}{dt} \right] dV - \int_V \delta\varepsilon^T m (s_o + p_o\xi) \frac{dp_o}{dt} dV =$$
$$\int_V \delta u^T \frac{df}{dt} dV + \int_S \delta u^T \frac{d\tau}{dt} dS \tag{1}$$

where D_{ep} is the elastic-plastic matrix, t is the time, $m = [1,1,1,0,0,0]^T$, K_s is the compressive modulus of solid particles, s_o is the liquid saturation of the rock, $\xi = \frac{ds_o}{dp_o}$ is the parameter of the relation between capillary pressure and saturation, p_o is the pore fluid pressure, ε is the strain, τ is the rock facial force, f is the rock physical force, $\delta\varepsilon$ is the virtual strain, δu is the virtual displacement, dV is the volume micro-element, and dS is the area micro-element.

Assuming that the seepage law in the rock is Darcy seepage, then the fluid seepage continuity equation can be obtained from the law of mass conservation [31]:

$$s_o \left(m^T - \frac{m^T D_{ep}}{3K_S} \right) \frac{d\varepsilon}{dt} - \nabla^T \left[k_0 k_r \left(\frac{\nabla p_o}{\rho_o} - g \right) \right] +$$
$$\left\{ \xi n + n \frac{s_o}{K_o} + s_o \left[\frac{1-n}{3K_S} - \frac{m^T D_{ep} m}{(3K_S)^2} \right] (s_o + p_o\xi) \right\} \frac{dp_o}{dx} = 0 \tag{2}$$

where k_0 is the product of the initial permeability coefficient tensor and fluid density, ρ_o is the liquid density, k_r is the specific permeability coefficient, g is the vector form of gravity acceleration, n is the rock porosity, K_o is the volume modulus of liquid in rock. $\nabla = \frac{\partial}{\partial x} \vec{i} + \frac{\partial}{\partial y} \vec{j} + \frac{\partial}{\partial x} \vec{k}$ is the three-dimensional vector differential operator or Nabla operator.

4.1.2. Boundary Conditions

(1) Traffic boundary conditions [32]:

$$-l^T k k_r \left(\frac{\nabla p_o}{\rho_o} - g \right) = q_o \tag{3}$$

where l is the unit normal direction of the flow boundary, k is the permeability coefficient tensor, and q_o is the total amount of fluid flowing through the boundary per unit of time.

(2) Pore pressure boundary conditions

The pore pressure boundary condition can be represented by $p_o = p_{ob}$, which means the pore pressure on the boundary is considered to be a certain value p_{ob}.

(3) Position boundary conditions

The boundary nodes in the X and Y directions are constrained, so that the node displacement is 0.

4.1.3. Finite Element Discretization Method and Stress-Seepage Coupling Equation

The shape function is defined as [32]:

$$\left. \begin{aligned} u &= N_u \overline{u} \\ \varepsilon &= B\overline{u} \\ p_o &= N_p \overline{p}_o \end{aligned} \right\} \tag{4}$$

where N_u and B are the vector matrix of the shape function, $\overline{u}$ is the element displacement, $\overline{p}_o$ is the unit node pore pressure, and N_p is the shape function.

$$\int_V a^T \overline{A} dV + \int_S b^T \overline{B} dS = 0 \tag{5}$$

where a and b are arbitrary functions, $\overline{A}$ is the governing equation, and $\overline{B}$ is the continuous boundary equation.

By substituting Equation (4) into Equation (1), the solid phase finite element formula can be simplified as:

$$K\frac{d\overline{u}}{dt} + C\frac{d\overline{p}_o}{dt} = \frac{df}{dt} \tag{6}$$

Transposing Equations (2) and (3), and making the right side of the equations be 0, the Galerkin method is then used to make the polynomials on the left side of Equations (2) and (3) replace $\overline{A}$ and $\overline{B}$ in Equation (5) respectively, and substitute the shape functions constructed by ε and p_o in Equation (4) into Equation (5). Making $a = -b$, the deformation formula is simplified as follows:

$$E\frac{d\overline{u}}{dt} + F\overline{p}_o + G\frac{d\overline{p}_o}{dt} = \widehat{f} \tag{7}$$

According to Equations (6) and (7), the stress-seepage coupling equation can be obtained:

$$\begin{bmatrix} K & C \\ E & G \end{bmatrix} \frac{d}{dt} \left\{ \begin{array}{c} \overline{u} \\ \overline{p}_o \end{array} \right\} + \begin{bmatrix} 0 & 0 \\ 0 & F \end{bmatrix} \left\{ \begin{array}{c} \overline{u} \\ \overline{p}_o \end{array} \right\} = \left\{ \begin{array}{c} \frac{df}{dt} \\ \widehat{f} \end{array} \right\} \tag{8}$$

Of which:

$$K = \int_V B^T D_{ep} B dV$$
$$C = \int_V B^T D_{ep} m \frac{(s_o + \xi p_o)}{3K_s} N_p dV - \int_V B^T (s_o + \xi p_o) m N_p dV$$
$$E = \int_V N_p{}^T \left[s_o \left(m^T - \frac{m^T D_{ep}}{3K_s} \right) B \right] dV$$
$$F = \int_V (\nabla N_p)^T k k_r \nabla N_p dV$$
$$G = \int_V N_p{}^T \left\{ s_o \left[\left(\frac{1-n}{K_s} - \frac{m^T D_{ep} m}{(3K_s)^2} \right) \right] \cdot (s_o + \xi p_o) + \xi n + n \frac{s_o}{K_o} \right\} N_p dV$$
$$df = \int_V N_u^T df dV + \int_S N_u^T d\tau dV$$
$$\overline{f} = \int_S N_u^T q_{ob} dS - \int_V (\nabla N_p)^T k k_r g dv$$

where q_{ob} is the fluid flow at the boundary.

4.1.4. Fracture Propagation and Fluid Flow Model

(1) Simulation of initial fractures

The extended finite element method was first proposed by Belytschko and Black [33]. A local enhancement function is incorporated into the traditional finite element method, and the presence of discontinuity is guaranteed by a special enhancement function and additional degrees of freedom. The displacement vector function (*u*) with the global enrichment function is approximately as follows [34]:

$$u = \sum_{I=1}^{N} N_I(x) \left[u_I + H_{(x)} a_I + \sum_{\alpha=1}^{4} F_\alpha(x) b_I^\alpha \right] \tag{9}$$

where $N_I(x)$ are the nodal shape functions, u_I is the nodal displacement vector with the continuous portion of the finite element solution, a_I and b_I^α are the nodal extension degrees of the freedom vector, $H_{(x)}$ is the Heaviside step function, $F_a(x)$ is the asymptotic displacement function of the fracture tip, and I is the nodal set of all the nodes in the mesh.

(2) Level-set simulation of fracture propagation

The level-set method can simulate the motion of the crack interface without the need of remeshing. This method updates the ϕ function by calculating the zero-level set intersection of the crack endpoint functions ψ and ϕ_i, so as to realize the simulation process of crack propagation.

The symbol distance function in the level-set method is usually expressed as:

$$\phi(X, t) = \pm \min_{X_r \in \gamma(t)} \|X - X_r\| \tag{10}$$

(3)   Criteria for initiation of the fracture

In this paper, the maximum principal stress criterion is used as the basis to judge the initial damage of materials. According to this criterion, when the maximum principal stress of a material exceeds a critical value, damage of the material begins to occur. The expression is:

$$f = \left\{ \frac{\langle \sigma_{\max} \rangle}{\sigma_{\max}^a} \right\} \tag{11}$$

where $\sigma_{\max}^a$ is the critical maximum principal stress. $\langle \sigma_{\max} \rangle$ is shown by the following:

$$\begin{cases} \langle \sigma_{\max} \rangle = 0, \sigma_{\max} < 0 \\ \langle \sigma_{\max} \rangle = \sigma_{\max}, \sigma_{\max} \geq 0 \end{cases} \tag{12}$$

where the Macaulay brackets indicate that the model will not be damaged under pure compressive stress.

(4)   Damage Evolution Criterion

According to the damage evolution of effective displacement, the damage variable D is positioned as:

$$D = \frac{\delta_m^f \left(\delta_m^{\max} - \delta_m^0 \right)}{\delta_m^{\max} \left(\delta_m^f - \delta_m^0 \right)} \tag{13}$$

where δ_m^f is the effective displacement at failure, which is considered as 0.001 m in this model, δ_m^0 is the effective displacements at the initial stage of damage evolution, and $\delta_m^{\max}$ is the maximum value of effective displacement during loading.

In the case of fluid–solid coupling in ABAQUS software, the seepage law of unfractured rock mass can be set as Darcy's law, while the fluid in a fracture is Newtonian fluid. The subcommand *Cflow is used to set the fluid in the fracture, and its flow law follows the pressure transfer formula of Newtonian fluid. Its expression is [32]:

$$Q = -k_t \nabla p \tag{14}$$

where k_t is the flow coefficient, which is related to the crack width and fluid viscosity.

4.2. Computational Model

As shown in Figure 12, considering the influence of vug size, horizontal stress difference and internal pressure within the vug on hydraulic fracture propagation, a 2D model was established. The size of the model to simulate the reservoir rock was 40 m × 40 m. An initial fracture with a length of 2 m long was placed in the center of the left boundary of the model. Meanwhile, a vug was set in the center of the model. Table 2 lists the basic parameters of the simulated reservoir. It should be noted that the fluid viscosity (50 mPa·s) and pumping rate (5 m³/min) refer to the field fracturing construction. While in laboratory scale, these parameters should be adjusted. Because the poured cement sample is more porous than the real reservoir formation, so the fluid viscosity was increased from 50 mPa·s to 100 mPa·s to counterbalance the filtration loss. At the same time, in order to achieve the quasi-static propagation of the hydraulic fracture, the pumping rate was reduced from 5 m³/min to 5 mL/min.
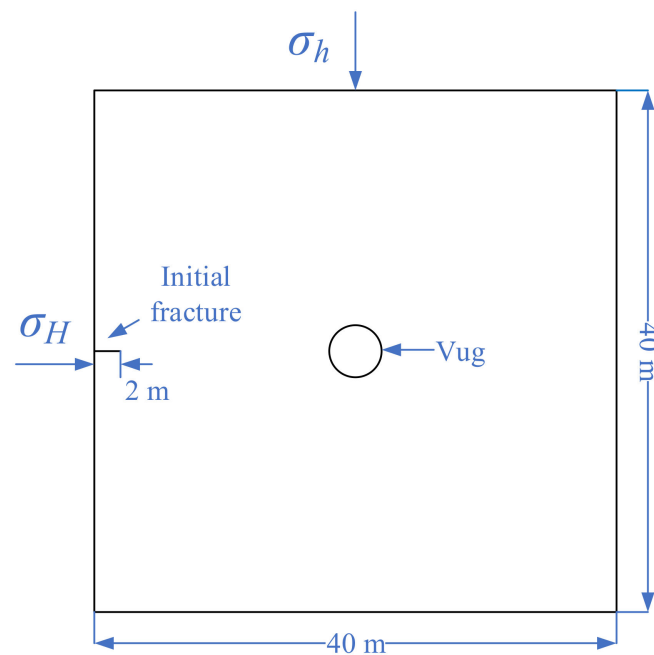
Figure 12. Numerical model schematic.

Table 2. Basic parameters of the simulated reservoir.

Parameter	Value			
Maximum horizontal principal stress σ_H (MPa)			75	
Minimum horizontal principal stress σ_h (MPa)	70	65	60	55
Young's modulus (GPa)			38.54	
Poisson's ratio			0.19	
Fluid viscosity (Pa·s)			0.05	
Pump rate (m³/min)			5	
Radius of the vug (m)	1	2	3	4
Pressure inside the vug (MPa)	65	60	55	50
Leak-off coefficient (m/Pa·s)			1^{-14}	
Permeability (mD)			0.11	

4.3. Results and Analysis

4.3.1. The Effect of Vug Size

To study the influence of vug size, four kinds of vug radius were simulated under the conditions that the horizontal maximum principal stress was 75 MPa, the horizontal minimum principal stress was 65 MPa, and the internal pressure of the vug was 50 MPa. As is shown in Figure 13a, the hydraulic fracture was arrested by the vug under the radius of 1 m. With the increase of the radius of the vug, the hydraulic fractures bypassed the vug during the process of extension (Figure 13b–d). With the increase of the vug radius, the range of stress concentration area caused by the vug increased, which affected the fracture propagation. When the radius increased to 4 m, the maximum deflection angle occurred.
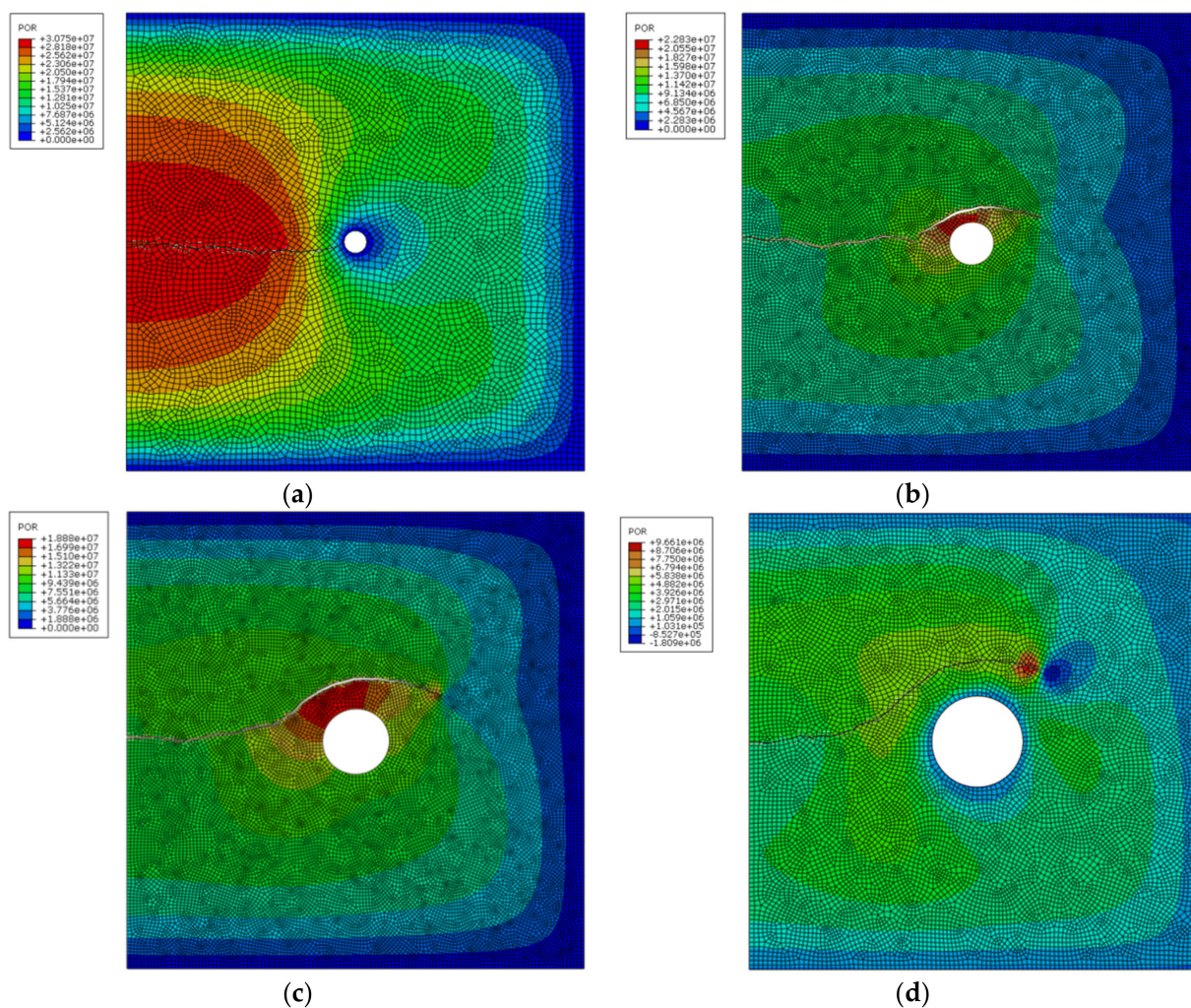
Figure 13. Cloud diagram of fracture propagation under different vug size: (**a**) R = 1 m; (**b**) R = 2 m; (**c**) R = 3 m; and (**d**) R = 4 m. (POR is the pore pressure. With the color gradually changing from red to blue, the pore pressure decreases.)

4.3.2. The Effect of Horizontal Stress Differences

In order to study the effect of horizontal stress differences, four cases of horizontal stress difference were investigated with a vug radius of 3 m and an inside vug pressure of 50 MPa. The hydraulic fractures bypassed the hole to expand when the horizontal stress difference was 5 MPa and 10 MPa (Figure 14a, b). As the stress difference increased to 15 MPa, the hydraulic fracture was stopped by the vug (Figure 14c). As illustrated in Figure 14d, when the stress difference continued to increase to 20 MPa, the hydraulic crack continued to expand through the vug.
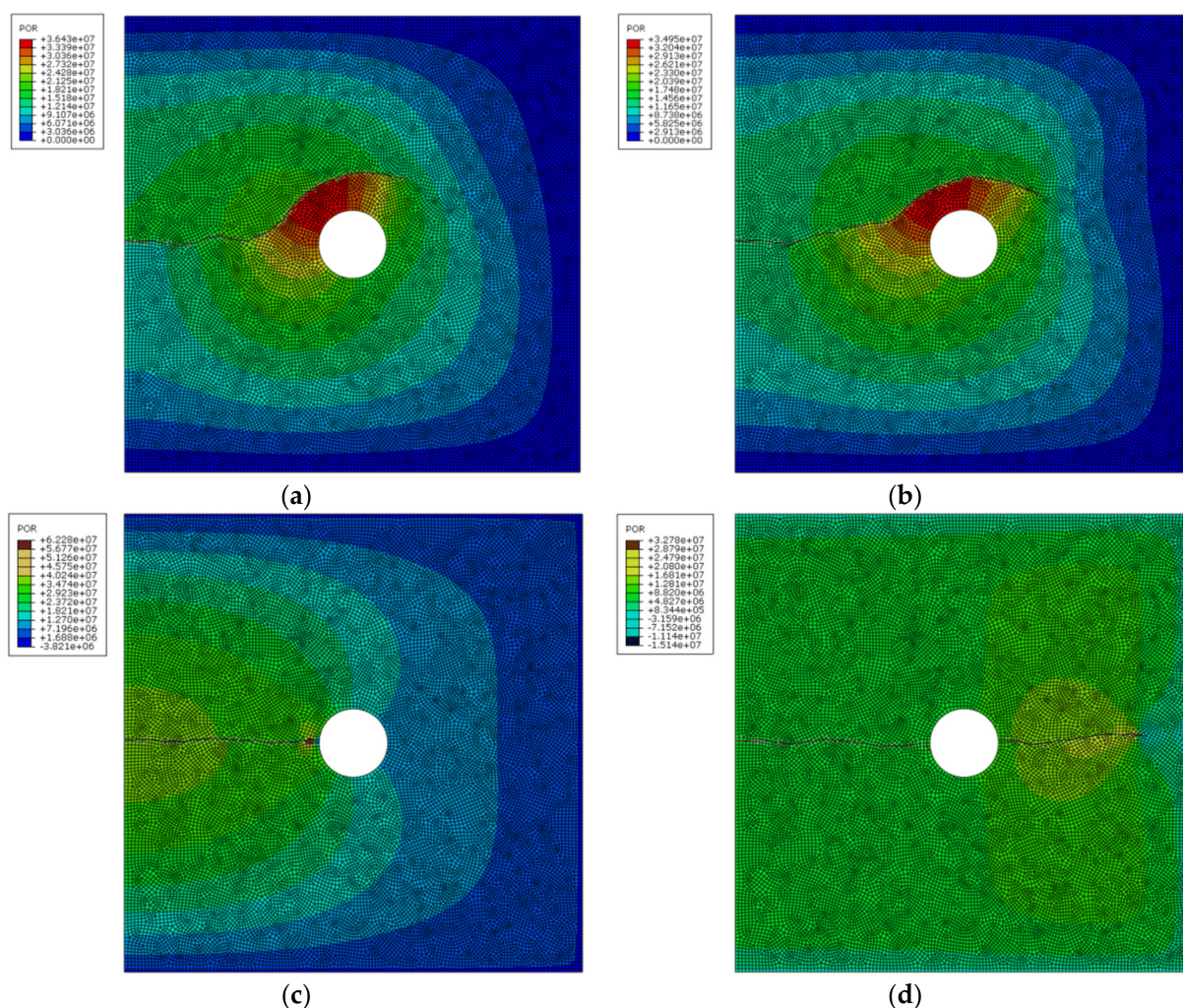
Figure 14. Cloud diagram of fracture propagation under different horizontal stress difference: (**a**) $\Delta\sigma$ = 5 MPa; (**b**) $\Delta\sigma$ = 10 MPa; (**c**) $\Delta\sigma$ = 15 MPa; and (**d**) $\Delta\sigma$ = 20 MPa. (POR is the pore pressure. With the color gradually changing from red to blue, the pore pressure decreases.)

4.3.3. The Effect of Internal Pressure in the Vug

In the field hydraulic fracturing operation, the internal pressure in the vug would have a large influence on the fracture extension. Since the indoor fractured samples are artificial specimens, it is impossible to simulate the changing conditions of the hole's internal pressure, so numerical simulation was used to study the effect of different internal hole pressure conditions on the fracture extension.

The effects of four types of internal hole pressures on crack extension were studied under the conditions of horizontal maximum principal stress of 75 MPa, horizontal minimum principal stress of 65 MPa, and hole radius of 3 m. The internal pressure difference was defined as the difference between the horizontal minimum principal stress and the internal pressure of the vug. As shown in Figure 15a,b, the hydraulic fractures bypassed the vug expansion when the internal pressure difference was 15 and 10 MPa. The fracture moved closer to the vug as the internal pressure difference decreased. When the internal pressure difference was 5 MPa, the expansion of the hydraulic fracture was stopped by the vug (Figure 15c). With an internal pressure difference of 0 MPa, as indicated in Figure 15d, the hydraulic fracture proceeded to extend directly through the hole. The smaller the internal pressure difference was, the easier the hydraulic fracture could overcome the stress concentration generated by the vug, and the easier it was to communicate with the vug.
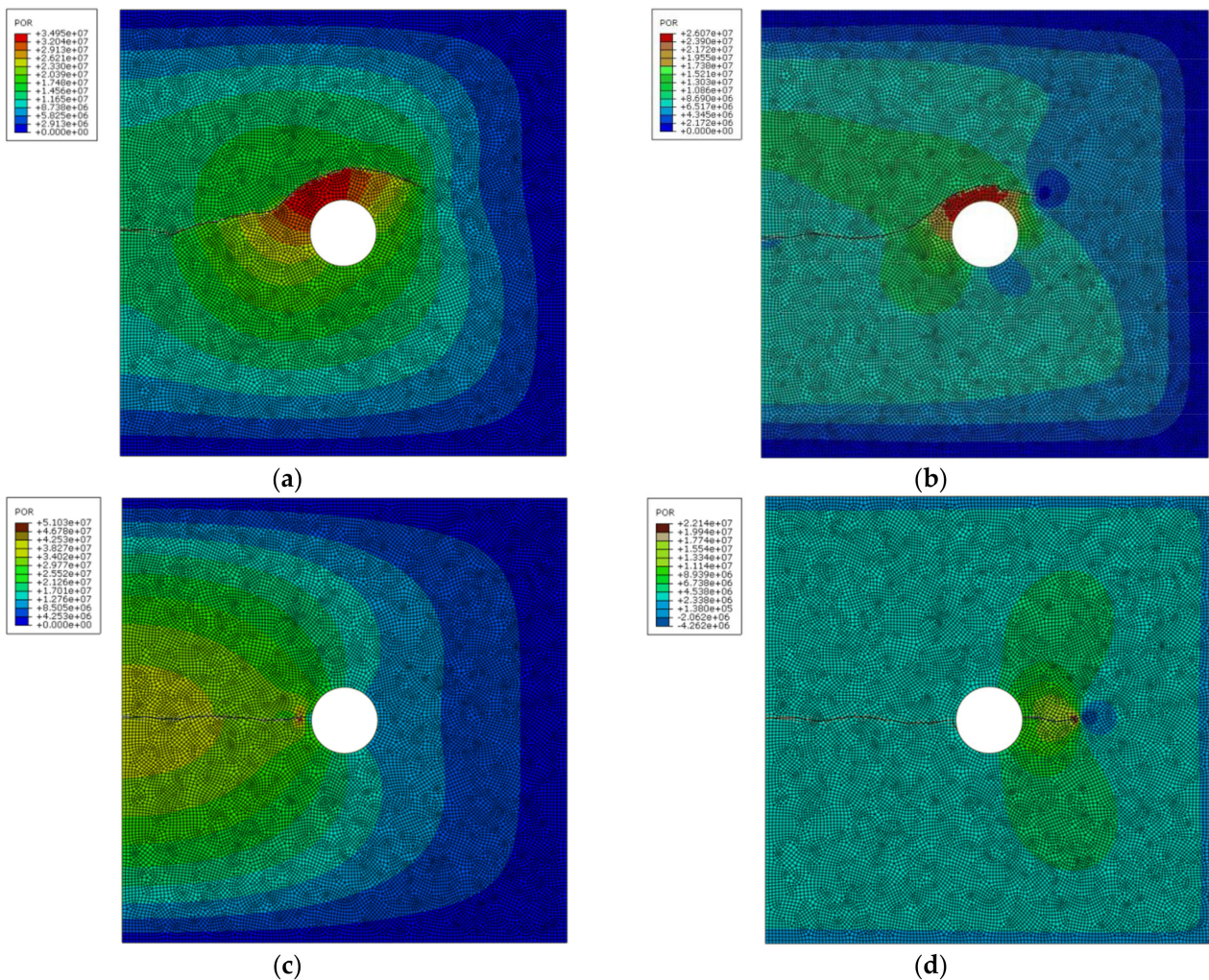
Figure 15. Cloud diagram of fracture propagation under different internal pressures of the vug: (**a**) P = 50 MPa; (**b**) P = 55 MPa; (**c**) P = 60 MPa; and (**d**) P = 65 MPa. (POR is the pore pressure. With the color gradually changing from red to blue, the pore pressure decreases.)

4.3.4. The Effect of Multiple Vugs

With multiple vugs in a carbonate reservoir, communicating with multiple vugs by hydraulic fracturing is the key issue in increasing production. The horizontal ground stress difference as the main control factor of hydraulic fracture expansion is also the primary influencing factor to be considered under the condition of multiple vugs. Therefore, three collinear vugs, with a radius of 1.5 m and internal pressure of 50 MPa, were set under four horizontal stress difference conditions.

As illustrated in Figure 16a, the hydraulic fracture bypassed the three collinear vugs and extended to the boundary at the horizontal stress difference of 5 MPa. After the horizontal stress difference increased to 10 MPa, the fracture was captured by the first vug and stopped expansion (Figure 16b). When the horizontal stress difference was 15 MPa, the fracture passed through the first vug, then bypassed the second and third vugs, and finally extended to the boundary. At the relatively high horizontal stress difference of 20 MPa, the hydraulic fracture crossed the first vug and was arrested by the second vug. From the results above, it was clear that the hydraulic fracture could communicate with more vugs as the horizontal stress difference became larger.
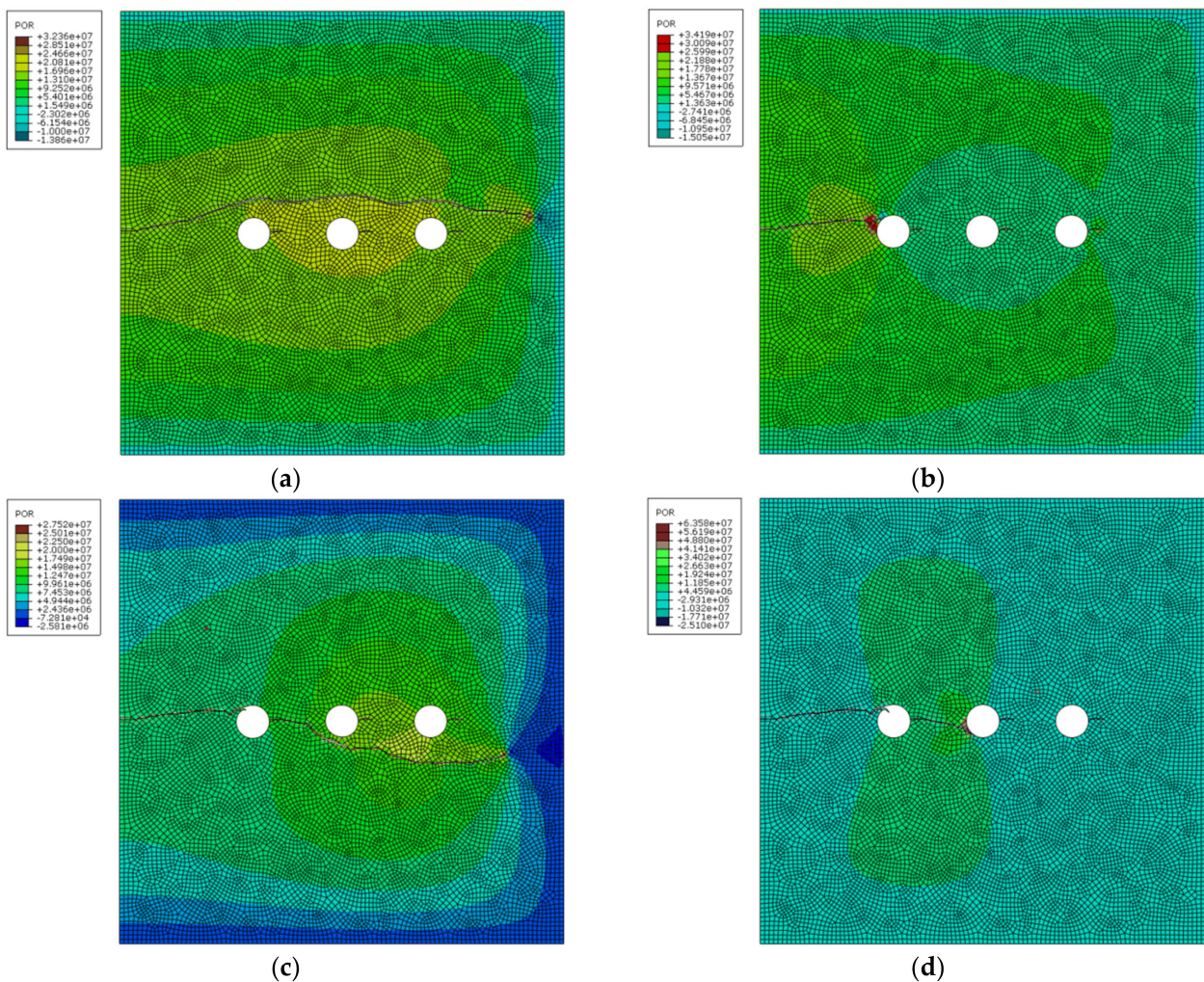
Figure 16. Schematic diagram of fracture propagation under different horizontal stress differences: (**a**) $\Delta\sigma$ = 5 MPa; (**b**) $\Delta\sigma$ = 10 MPa; (**c**) $\Delta\sigma$ = 15 MPa; and (**d**) $\Delta\sigma$ = 20 MPa. (POR is the pore pressure. With the color gradually changing from red to blue, the pore pressure decreases.)

5. Conclusions

Aiming at improving the stimulation effect of the fracture–vug carbonate reservoir, the interaction between vugs and hydraulic fractures was investigated, from the perspectives of laboratory hydraulic fracturing tests and numerical simulations. The following conclusions were obtained.

(1) Vugs play an important role in the propagation of hydraulic fractures. Three modes of vug–hydraulic fracture interaction were observed in both laboratory and numerical tests: crossing, arresting, and bypassing.

(2) The stress concentration phenomenon exists around the vug and increases with the increase of vug size. The hydraulic fracture could be arrested by the small vug but would bypass the vug of a larger size.

(3) Whether the hydraulic fracture could communicate with the vug is mainly controlled by the horizontal stress difference. With large horizontal stress differences ($\geq$20 MPa), the hydraulic fracture could cross and connect multiple vugs.

(4) The difference between the horizontal minimum stress and the internal pressure of the vug is also particularly significant for fracture propagation. The smaller the difference, the easier the fracture communicates with the vug.

References

1. Kossack, C.A.; Gurpinar, O. A Methodology for Simulation of Vuggy and Fractured Reservoirs. In Proceedings of the SPE Reservoir Simulation Symposium, Houston, TX, USA, 11–14 February 2007. [CrossRef]
2. Hidajat, I.; Mohanty, K.K.; Flaum, M.; Hirasaki, G. Study of Vuggy Carbonates Using NMR and X-Ray CT Scanning. *SPE Reserv. Eval. Eng.* **2004**, *7*, 365–377. [CrossRef]
3. Roehl, P.O.; Choquette, P.W. *Carbonate Petroleum Reservoirs*; Springer: Berlin/Heidelberg, Germany, 1985. [CrossRef]
4. Lucia, F.J. *Carbonate Reservoir Characterization*; Springer: Berlin/Heidelberg, Germany, 2007.
5. Jeon, J.; Bashir, M.O.; Liu, J.; Wu, X. Fracturing Carbonate Reservoirs: Acidising Fracturing or Fracturing with Proppants? In Proceedings of the SPE Asia Pacific Hydraulic Fracturing Conference, Beijing, China, 24–26 August 2016.
6. Suleimenova, A.; Wang, X.; Zhu, D.; Hill, A.D. Comparative Study of Acid Fracturing and Propped Hydraulic Fracturing for a Tight Carbonate Formation. In Proceedings of the SPE Europec featured at 78th EAGE Conference and Exhibition, Vienna, Austria, 30 May–2 June 2016.
7. Velazquez, R.C.; Vasquez-Cruz, M.A.; Castrejon-Aivar, R.; Arana-Ortiz, V. Pressure Transient and Decline Curve Behaviors in Naturally Fractured Vuggy Carbonate Reservoirs. *SPE Reserv. Eval. Eng.* **2005**, *8*, 95–112. [CrossRef]
8. Kang, Z.; Wu, Y.S.; Li, J.; Wu, Y.; Wang, G. Modeling Multiphase Flow in Naturally Fractured Vuggy Petroleum Reservoirs. In Proceedings of the SPE Annual Technical Conference and Exhibition, San Antonio, TX, USA, 24–27 September 2006.
9. Wu, Y.S.; Harasaki, K. Conceptualization and Modeling of Flow and Transport Through Fault Zones. In Proceedings of the Latin American and Caribbean Petroleum Engineering Conference, Cartagena de Indias, Colombia, 31 May–30 June 2009.
10. Li, C.; Zhou, X.; You, S.; Ibragimov, J.J. Analysis of Two-Phase Gas–Water Flow in Carbonate Reservoirs. *J. Min. Sci.* **2018**, *53*, 643–654. [CrossRef]
11. Asadollahpour, E.; Baghbanan, A.; Hashemolhosseini, H.; Mohtarami, E. The etching and hydraulic conductivity of acidized rough fractures. *J. Pet. Sci. Eng.* **2018**, *166*, 704–717. [CrossRef]
12. Liu, B.; Jin, Y.; Chen, M. Influence of vugs in fractured-vuggy carbonate reservoirs on hydraulic fracture propagation based on laboratory experiments. *J. Struct. Geol.* **2019**, *124*, 143–150. [CrossRef]
13. Liu, Z.; Tang, X.; Tao, S.; Zhang, G.; Chen, M. Mechanism of Connecting Natural Caves and Wells Through Hydraulic Fracturing in Fracture-Cavity Reservoirs. *Rock Mech. Rock Eng.* **2020**, *53*, 5511–5530. [CrossRef]
14. Bittencourt, T.N.; Wawrzynek, P.A.; Ingraffea, A.R.; Sousa, J.L. Quasi-automatic simulation of crack propagation for 2D LEFM problems. *Eng. Fract. Mech.* **1996**, *55*, 321–334. [CrossRef]
15. Phongthanapanich, S.; Dechaumphai, P. Adaptive Delaunay triangulation with object-oriented programming for crack propagation analysis. *Finite Elem. Anal. Des.* **2004**, *40*, 1753–1771. [CrossRef]
16. Häusler, S.M.; Lindhorst, K.; Horst, P. Combination of the material force concept and the extended finite element method for mixed mode crack growth simulations. *Int. J. Numer. Methods Eng.* **2011**, *85*, 1522–1542. [CrossRef]
17. Sukumar, N.; Chopp, D.L.; Mo?S, N.; Belytschko, T. Modeling holes and inclusions by level sets in the extended finite-element method. *Comput. Methods Appl. Mech. Eng.* **2001**, *190*, 6183–6200. [CrossRef]
18. Zhao, H.; Xie, Y.; Zhao, L.; Liu, Z.; Li, Y.; Li, N. Simulation of Mechanism of Hydraulic Fracture Propagation in Fracture-Cavity Reservoirs. *Chem. Technol. Fuels Oils* **2020**, *55*, 814–827. [CrossRef]
19. Wang, Y.; Zhang, Z.; Mu, J.; Zhao, B.; Liu, Z. Impact of Cavity on Hydraulic Fracture in cavity Carbonate Reservoir. *Chin. J. Undergr. Space Eng.* **2019**, *15*, 175–181.
20. Shi, F.; Wang, D.; Chen, X. A numerical study on the propagation mechanisms of hydraulic fractures in fracture-cavity carbonate reservoirs. *C.-Comput. Model. Eng. Sci.* **2021**, *127*, 575–598. [CrossRef]
21. Luo, Z.; Zhang, N.; Zhao, L.; Zeng, J.; Liu, P.; Li, N. Interaction of a hydraulic fracture with a hole in poroelasticity medium based on extended finite element method. *Eng. Anal. Bound. Elem.* **2020**, *115*, 108–119. [CrossRef]
22. Wang, Y.; Li, X.; Zhao, B.; Zhang, Z. 3D numerical simulation of pulsed fracture in complex fracture-cavitied reservoir. *Comput. Geotech.* **2020**, *125*, 103665. [CrossRef]
23. Kao, J.; Wang, W.; Jin, Y.; Liu, H. Numerical Simulation and Analysis of Cave Penetration by Hydraulic Fractures. *IOP Conf. Ser. Earth Environ. Sci.* **2020**, *570*, 022029. [CrossRef]

24. Zhou, L.; Guo, A.; Wang, X.; Qiao, J.; Tang, X. The effect of temperature, natural fractures and vugs on the acidizing process in fractured-vuggy reservoirs with hydro-thermal-chemical coupled modeling. *J. Pet. Sci. Eng.* **2022**, *213*, 110416. [CrossRef]
25. Beugelsdijk, L.J.L.; Pater, C.; Sato, K. Experimental Hydraulic Fracture Propagation in a Multi-Fractured Medium. In Proceedings of the SPE Asia Pacific Conference on Integrated Modelling for Asset Management, Yokohama, Japan, 25–26 April 2000.
26. Bai, Q.; Tu, S.; Wang, F.; Zhang, C. Field and numerical investigations of gateroad system failure induced by hard roofs in a longwall top coal caving face. *Int. J. Coal Geol.* **2017**, *173*, 176–199. [CrossRef]
27. Zhang, Z.; Bai, J.; Chen, Y.; Yan, S. An innovative approach for gob-side entry retaining in highly gassy fully-mechanized longwall top-coal caving. *Int. J. Rock Mech. Min. Sci.* **2015**, *80*, 1–11. [CrossRef]
28. Cheng, Y.; Lu, Y.; Ge, Z.; Liang, C.; Zhang, W. Experimental study on crack propagation control and mechanism analysis of directional hydraulic fracturing. *Fuel* **2018**, *218*, 316–324. [CrossRef]
29. Bai, Q.; Liu, Z.; Zhang, C.; Wang, F. Geometry nature of hydraulic fracture propagation from oriented perforations and implications for directional hydraulic fracturing. *Comput. Geotech.* **2020**, *125*, 103682. [CrossRef]
30. Zhang, X.Y.; Dai, Z.H. Analysis of slope stability under seepage by using ABAQUS program. *Chin. J. Rock Mech. Eng.* **2010**, *29* Suppl. S1, 2927–2934.
31. Li, P.C. Mathematical models of flow-deformation coupling for porous media. *Chin. J. Rock Mech. Eng.* **2004**, *23*, 2842.
32. Gong, D.; Qu, Z.; Li, J.; Qu, G.; Cao, Y.; Guo, T. Extended finite element simulation of hydraulic fracture based on ABAQUS platform. *Rock Soil Mech.* **2016**, *37*, 1512–1520.
33. Belytschko, T.; Black, T. Elastic crack growth in finite elements with minimal remeshing. *Int. J. Numer. Methods Eng.* **1999**, *45*, 601–620. [CrossRef]
34. Han, W.; Cui, Z.; Zhang, J. Fracture path interaction of two adjacent perforations subjected to different injection rate increments. *Comput. Geotech.* **2020**, *122*, 103500. [CrossRef]